Check for updates

Real roles of perylene diimides for improving photocatalytic activity†

Fengxia Zhang,* Wenjing Li, Tianyi Jiang, Xuemei Li, Yuanyuan Shao, Yongshan Ma ⓘ* and Junsen Wu*

Three novel visible-light-driven composite photocatalysts: five-membered O-heterocyclic annulated perylene diimide doped TiO₂ (**PDI-1**/TiO₂), 1-phenol-*N*,*N*′-dicyclohexyl perylene-3,4,9,10-tetracarboxylic diimide doped TiO₂ (**PDI-2**/TiO₂), and *N*,*N*′-dicyclohexyl perylene diimide doped TiO₂ (**PDI-3**/TiO₂), were synthesized using a hydrothermal synthesis method. The effects of introducing PDIs with different structures into TiO₂ were evaluated by assaying the photodegradation rate of Methylene Blue (MB). The photoactivities of the **PDI-1**/TiO₂ and **PDI-2**/TiO₂ catalysts were better than that of **PDI-3**/TiO₂. This is because the large surface area of **PDI-1** nanorods and **PDI-2** nanobelts extended the 1D charge carrier channel, which facilitated electron transfer to the TiO₂ surface and improved the photocatalytic activity of the composites. The **PDI-1**/TiO₂ composite showed the highest photoactivity, and the activity remained at 86.4% after four reuse cycles. The extended π–π stacking of self-assembled **PDI-1** and the strong interactions between self-assembled **PDI-1** and TiO₂ played significant roles in accelerating charge transfer and decreasing recombination of photogenerated electron–hole pairs. The steric hindrance of the phenoxy substituent at the bay position of **PDI-2** prevented the **PDI-2** nucleus from contacting TiO₂ and weakened the interaction between **PDI-2** and TiO₂, which further resulted in the low photoactivity of **PDI-2**/TiO₂. This work provides a practical way to improve the performances of traditional organic and inorganic composite photocatalysts.

1. Introduction

Perylene tetracarboxylic diimide and its derivatives (PDIs) are considered to be good n-type organic semiconductor materials because of their excellent optical and thermal stabilities, excellent optical trapping abilities, and carrier transport properties.[1,2] PDIs have high electron affinities and electron mobilities due to the strong π–π stacking between conjugated π-bonds. Therefore, they have been extensively used as fluorescent and near-infrared dyes, or as organic field effect transistors and photodiodes.[3,4] The special fused-ring structures and strong intermolecular forces of PDIs make them poorly soluble, and they have high electron–hole recombination. These properties have limited their applications in photocatalysis.[5]

Modifications of the molecular structures of PDIs were usually achieved by introducing substituents into the imine nitrogen atoms or at bay locations.[6,7] Substitutions at the imine position can increase the solubilities of PDIs in organic solvents and facilitate the assembly of PDI molecules into nanostructures. However, such substitutions can not affect the properties and electronic structures of PDIs because the nodes in both highest occupied molecular orbital (HOMO) and lowest unoccupied molecular orbital (LUMO) levels will limit the electronic interactions between substituents and perylene core.[8] Substitutions at the bay position can also increase the solubilities of PDIs in organic solvents. In addition, such substitutions often result in distortion of the perylene core, which alters the photo-physical properties of PDIs.[9] Moreover, phenol was often selected as a soluble group due to its flexibility and low steric resistance, and so it has a slight effect on intermolecular proximity and π–π stacking of adjacent PDIs. Sometimes phenoxy substituents can also facilitate the perylene molecules to self-assemble into ordered structure. The planar molecular geometries of PDIs with phenoxy substituents gave them high charge carrier mobilities, which could be a premise of efficient photoelectronic and organic electronic devices.[10] As important structural motifs, fully fused bay-modifications of PDIs have received extensive attention and such fusions have been shown to provide excellent electronic and photoelectronic properties.[11] The extension along the short molecular axis of perylene core caused a shift in the absorption spectrum and a variety of intermolecular interactions. These interactions are critical for achieving highly ordered supramolecular self-assembled structure which can enhance device performance.[12] Introducing heteroatom into a π-conjugated system is also an easy way to

School of Municipal and Environmental Engineering, Shandong Jianzhu University, Jinan 250101, Shandong, China. E-mail: zhangfengxia19@sdjzu.edu.cn; mlosh@sdjzu.edu.cn; wujunsen@sdjzu.edu.cn

construct intramolecular charge transfer compounds because the lone pair electrons of the heteroatom can be used as electron donors.[13]

Photocatalysis has received increasing attention due to its application in organic pollutants decomposing, water photosplitting, and waste water treatment.[14] Photocatalytic materials such as TiO_2, ZnO, g-C_3N_4, metallophalocyanine (MPc), and their composites have been widely used.[15–19] Among the reported photocatalytic materials, TiO_2 is considered as an effective catalyst for the degradation of organic pollutants because it is non-toxic, inexpensive, and chemically stable. However, TiO_2 has low visible light utilization efficiency and high electron–hole recombination efficiency, which limit its large-scale application.[20] Surface adjustment strategies and modifications have been applied to TiO_2 to increase its photocatalytic activity. For example, TiO_2 doped with C, N, or metal particles exhibited improved catalytic activities. However, the response range of visible light did not increase significantly, and the charge recombination center can also be easily introduced for these modified TiO_2.[21] Therefore, they were still insufficient for practical applications.

Compared to traditional inorganic semiconductors, organic semiconductors have advantages like high flexibility, chemical structure diversity, and low cost. Introducing visible light active organic materials (such as PDIs) into TiO_2 should be a possible approach to improve its solar photocatalytic activity.[22,23] The main advantage of this method, similar to dye-sensitized nanocrystalline titanium dioxide solar cells, is that the interfacial area between the p- and n-type materials was greatly increased, and this change can improve the charging efficiency and the utilization rate of solar radiation. The low electron–hole recombination can also be improved by doping PDIs on TiO_2. For example, Zang *et al.* deposited TiO_2 layers on the 1D self-assembled nanofibers of PDIs *in situ*, which enhanced its hydrogen production activity.[24] Nagarajan *et al.* synthesized N,N'-di(octadecyl)perylene-3,4,9,10-tetracarboxylic bisimide and TiO_2 as a semiconductor material with π-conjugated structure and it could accelerate electron transfer during the degradation of Reactive Orange 4.[25] Zhu *et al.* used TiO_2 colloid and compound nanowires PDIs colloid under acidic conditions to improve the photocatalytic degradation activity towards organic pollutants.[26] Cui *et al.* enhanced the photocatalytic degradation activity towards organic pollutants through self-assembly perylene tetracarboxylic acid diimide polymer nanostructures incorporating TiO_2 nanoparticles.[27] However, few literatures reported photocatalyst materials with bay area substituted PDIs, although such substituents can significantly change the electronic structures and photochemical properties of PDIs. It is because that this kind of PDIs was difficult to form well-defined nanostructures due to the distortion of π–π stacking.[28–30] The researches on the mechanism of promoting photo-induced charge transfer by PDIs are still insufficient, and the separation efficiencies of electron and hole of the semiconductor catalysts are still low.

Here, we designed and synthesized three novel visible-light-driven composite photocatalysts: five-membered O-heterocyclic annulated perylene diimide doped TiO_2 (PDI-1/TiO_2), 1-phenol-
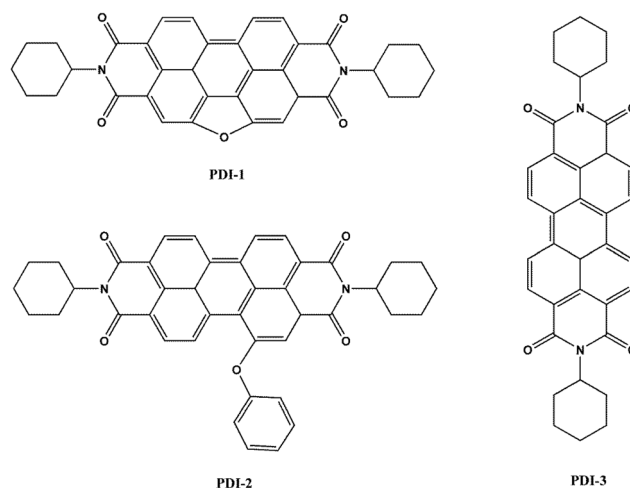

Fig. 1 Chemical structures of PDI-1, PDI-2 and PDI-3 molecules.

N,N'-dicyclohexyl perylene-3,4,9,10-tetracarboxylic diimide doped TiO_2 (PDI-2/TiO_2) and N,N'-dicyclohexyl perylene diimide doped TiO_2 (PDI-3/TiO_2) (Fig. 1). These composites were prepared by hydrothermal synthesis method. Optical properties and electronic structures of PDI-1, PDI-2, and PDI-3, nanostructure morphology, absorption, fluorescence, surface chemical properties, crystalline structure, and stability of PDI-1/TiO_2, PDI-2/TiO_2 and PDI-3/TiO_2, and binding energy of PDI-1, PDI-2 and PDI-3 with TiO_2 have been investigated. Also, the photocatalytic activities of PDI-1/TiO_2, PDI-2/TiO_2 and PDI-3/TiO_2 have been tested by degrading Methylene Blue (MB) under visible light.

2. Experimental and characterization

2.1. Materials and measurements

All reagents and solvents were analytically pure, purchased from commercial sources and used without further purification. The synthesis of bay unilaterally extended PDI-1 and bay phenoxy mono-substituted PDI-2 was performed according to our literatures procedure with yields of *ca.* 30% and 90%, respectively.[31,32] The synthetic routes of PDI-1 and PDI-2 (Fig. S1†) along with their characterization data are reported in the ESI Methods.† ^{1}H NMR and ^{13}C NMR spectra were measured with a Bruker Advance 400 spectrometer in $CDCl_3$ at room temperature. FT-IR spectrum was taken on a Bruker Tensor-27 spectrophotometer. Mass spectra were recorded in a Bruker Maxis UHR-TOF mass spectrometer. Absorption spectra and fluorescence measurements were performed at a Varian CARY-50 spectrophotometer and a Hitachi FL-4500 spectrometer. Cyclic voltammetry was recorded at a CHI760E electrochemical analyzer using three electrode cell units, Pt as counter electrode, glassy carbon working electrode and Ag/$AgNO_3$ reference electrode. Tetrabutylammonium perchlorate (Bu_4NClO_4) was used as a supporting electrolyte, the scan rate employed was 100 mV s^{-1} and the current sensitivity was given as 0.01 μA. Scanning electron microscopy (SEM) images were obtained on a FEI NOVA NANOSEM 450 microscope. The specific surface area of

the catalyst was analyzed using nitrogen adsorption at 77 K applying the BET (Brunauer–Emmett–Teller) method using a micrometrics ASAP 2020 V3.00 H. X-ray diffraction (XRD) measurements were performed using a Rigaku R-AXIS RAPID X-ray diffractometer. The ultraviolet-visible diffuse reflectance absorption spectra (DRS) were measured on a Shimadzu model UV-Vis diffuse reflectance spectrometer. X-ray photoelectron spectroscopy (XPS) was performed on a KRATOS model XSAM800 instrument. The quantum yields in the solid states were measured with the Hamamatsu spectrometer C11347 Quantaurus-QY. Fluorescence lifetimes were measured with the Hamamatsu spectrometer C11367. Both structure optimization and the property calculations were performed using Density Function Theory with B3LYP hybrid method and the standard 6-31G* basis set with the Gaussian 03 program package.[33–35] The Mott–Schottky plots, photocurrent, and electrochemical impedance spectroscopy (EIS) were measured on a CHI760E electrochemical workstation using a three-electrode system. ITO deposited by photocatalyst was used as working electrodes, platinum wire as counter electrode, saturated calomel as reference electrode, and 0.1 M Na_2SO_4 aqueous solution was used as electrolyte. The photoelectric response of the sample was measured at 0.0 V, and the EIS was performed at an open circuit potential at a frequency of 0–10 000 Hz.

2.2. Preparation of PDIs loaded TiO_2 photocatalyst

The 0.01 wt% **PDI-1** loaded TiO_2 (**PDI-1**/TiO_2) composite was prepared by the hydrothermal synthesis method, taking tetra-butyl titanate as the starting material. 10 mL of tetrabutyl titanate was dissolved in 30 mL of anhydrous ethanol and to this solution 5 mL of water was added dropwise under vigorous stirring. Then 10 mg of **PDI-1** dissolved in 5 mL of dichloromethane was added dropwise for 20 minutes under sonication. The resulting colloidal suspension was stirred for 12 h and then transfer to the hydrothermal kettle at 200 °C for 3 h. The composite obtained was filtered and dried in an air oven at 100 °C for 4 h. This catalyst contained 0.01 wt% of **PDI-1**. The 0.01 wt% **PDI-2** loaded TiO_2 (**PDI-2**/TiO_2), 0.01 wt% **PDI-3** loaded TiO_2 (**PDI-3**/TiO_2), 0.005 wt% of **PDI-1** loaded TiO_2 (0.005 wt% **PDI-1**/TiO_2), 0.02 wt% of **PDI-1** loaded TiO_2 (0.02 wt% **PDI-1**/TiO_2) and pure TiO_2 were prepared using the same procedure.

2.3. Irradiation procedure

A photochemical reactor (PhchemIII, Beijing, China NBeT) was used for the degradation by visible light. The visible light source is obtained by a 500W xenon lamp (XE-JY500) with cutoff filter (>420 nm). It has a reaction chamber with a specially designed reflector made of highly polished aluminium and a built-in cooling fan. It also provides a magnetic stirrer and 50 mL reactive quartz tubes. The light exposure length is 230 mm. The photodegradation reactions were carried out in quartz tube reactor with a 50 mL 10 mg L^{-1} MB solution and 50 mg photocatalyst powders. The reaction temperature was held at 25 °C with magnetic stirring.

The suspension solutions were stirred for 30 min in dark prior to illumination in order to reach the adsorption–desorption equilibrium. At given time intervals, 2.0 mL of the sample were withdrawn and centrifuged to remove the photo-catalysts. The changes in the concentration of MB were monitored by UV-visible spectrophotometer from its characteristic absorptions at 291 nm and 664 nm. The absorbance at 664 nm is used to monitor the decolourization of MB, while the absorbance at 291 nm represents the aromatic part of MB and its decrease indicates the degradation of the aromatic part of the dye.

3. Results and discussion

3.1. Photocatalytic activity

The photocatalytic activity of **PDI-1**/TiO_2, **PDI-2**/TiO_2, and **PDI-3**/TiO_2 were tested by degrading Methylene Blue (MB: C.I. no. 52015, molecular formula: $C_{16}H_{18}ClN_3S$, molecular weight: 319.85), which has been extensively used in dyeing industry. Its structure and UV-visible spectra are shown in Fig. S9.†

Photocatalytic degradation and decolorization of MB with pure TiO_2, **PDI-1**/TiO_2, **PDI-2**/TiO_2, and **PDI-3**/TiO_2 under visible light are shown in Fig. 2. There was negligible degradation (about 0.3%) when the dye solution was irradiated without a catalyst. In the same experiment with **PDI-1**/TiO_2 in the absence of light, the removal rate of MB was 3.5%, which may be due to the adsorption of dye on the catalyst (Fig. 2a). MB dye underwent 96.4% degradation and 98.1% decolorization in the presence of **PDI-1**/TiO_2 under visible light irradiation for 120 min. These observations indicate that both light and photocatalyst were necessary to effectively degrade MB. The corresponding data was 78% and 93% for **PDI-2**/TiO_2, and 73.9% and 72.4% for **PDI-3**/TiO_2. Comparatively, only 64.1% degradation and 71% decolorization occurred with pure TiO_2 as catalyst (Fig. 2b). Though TiO_2 had no visible light absorption, it had been found to be solar active. This may be due to the higher adsorption of MB dye on the TiO_2, which favored the presence of dye sensitization mechanism. These data show that the photocatalytic activity of the hybrid photo-catalyst **PDI-1**/TiO_2 was obviously higher than that of other catalysts.

Fig. 2c showed the photocatalytic degradations of MB with 0.005 wt% or 0.02 wt% **PDI-1**/TiO_2 under visible light irradiation for 120 min. Only 67.8% degradation and 79.5% decolorization of MB were observed with 0.005 wt% **PDI-1**/TiO_2, whereas no significant change was observed with 0.02 wt% **PDI-1**/TiO_2. The results showed that 0.01 wt% **PDI-1**/TiO_2 had higher efficiency in MB degradation than other catalysts. For comparison, the pseudo-first order degradation rate constants of several common photocatalysts under the same conditions are also listed in ESI in Table S1.†

3.2. Characterization of catalyst

We were interested in why the 0.01 wt% **PDI-1**/TiO_2 composite could gain the strongest oxidation ability and why the activity declined when **PDI-1** was replaced by **PDI-2** and **PDI-3**. The properties of these materials were determined by different PDIs molecular properties. To explain these results, the optical properties and electronic structures of the three PDIs were
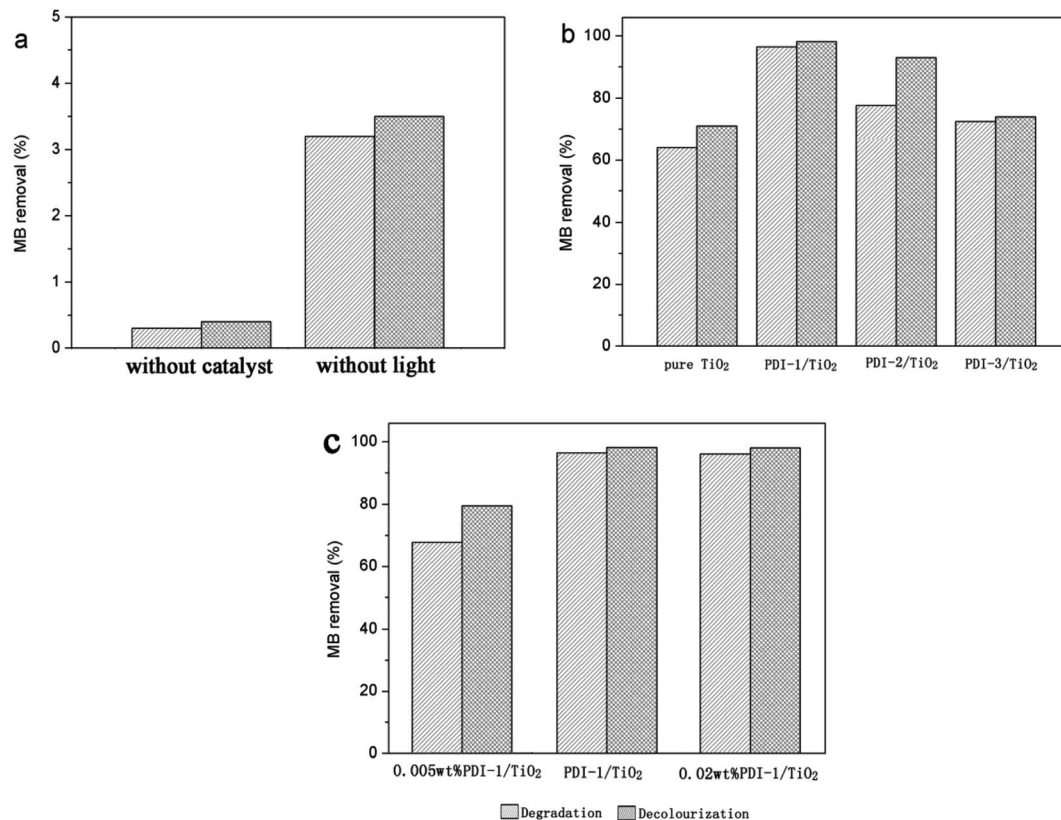
Fig. 2 Photodegradation and decolourization of MB: (a) without catalyst or without light; (b) different photocatalysts; and (c) PDI-1/TiO$_2$ composite photocatalysts with different PDI-1 mass ratio. [MB] = 10 mg L^{-1}, pH = 7, catalyst suspended = 1 g L^{-1}, irradiation time = 120 min.

studied, and the morphologies of materials were observed to illuminate their internal structures.

The optical properties of compounds PDI-1, PDI-2, and PDI-3 in dichloromethane were studied by UV-Vis and fluorescence spectra (Fig. 3). The spectra of PDI-3 showed two absorption bands (524 nm and 487 nm) and a shoulder peak at approximately 456 nm, which were consistent with the transition energy characteristics of 0–0, 0–1, and 0–2.[36] The absorption

peaks of PDI-1 appeared at 512 nm and 478 nm with a shoulder around 448 nm, which were blue shifted compared with PDI-3, reflecting the extension of aromatic nucleus on the short molecular axis.[37] The maximum absorption peak of PDI-2 (558 nm) was red-shifted relative to PDI-1 and PDI-3. This change may be caused by the distortion of the PDI nucleus, or by the electronic coupling between the electron-rich substituent and the electron-deficient PDI nucleus.[38] The fluorescence emission peaks appeared at 520 nm, 560 nm, and 535 nm for PDI-1, PDI-2, and PDI-3 with corresponding Stokes shifts of 8 nm, 32 nm, and 11 nm, respectively.

The absorption spectra of PDI-1, PDI-2, and PDI-3 in dichloromethane at various concentrations are shown in Fig. S10.† For a free monomer, the normal progression of its Franck–Condon factor was $A^{0-0} > A^{0-1} > A^{0-2}$. However, as the monomers begin to aggregate, the 0–1 transition will increase.[31] The 0–1 transition absorptions of PDI-2 (from 5.0 × 10^{-6} to 2.0 × 10^{-5} mol L^{-1}) and PDI-3 (from 5.0 × 10^{-6} to 4.0 × 10^{-5} mol L^{-1}) increased obviously (Fig. S11a and b†). However, the absorption of PDI-1 (from 5.0 × 10^{-6} to 2.0 × 10^{-5} mol L^{-1}) did not show any increase (Fig. S11a†). These results indicated that aggregation occurred for PDI-2 and PDI-3 but didn't occur for PDI-1 at low concentration, and the solubility of PDI-1 was better than that of PDI-2 and PDI-3 in common organic solvent.

Optimized structures and computed frontier orbitals of PDI-1, PDI-2, and PDI-3 are shown in Fig. 4. The results show that
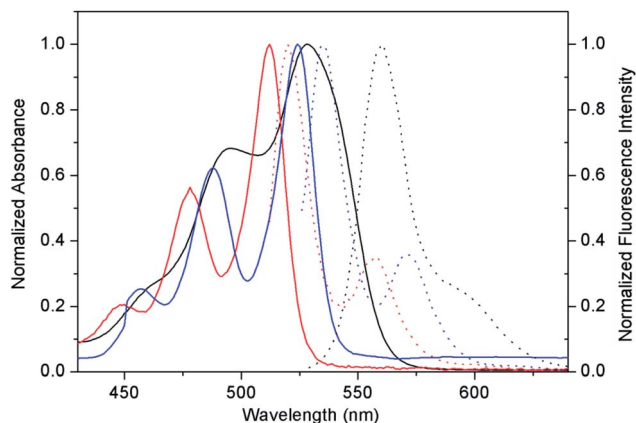

Fig. 3 Optical properties of PDI-1, PDI-2, and PDI-3. Absorption spectra (solid lines) and corresponding fluorescence spectra (dot lines) of PDI-1 (red), PDI-2 (black), and PDI-3 (blue) in dichloromethane.
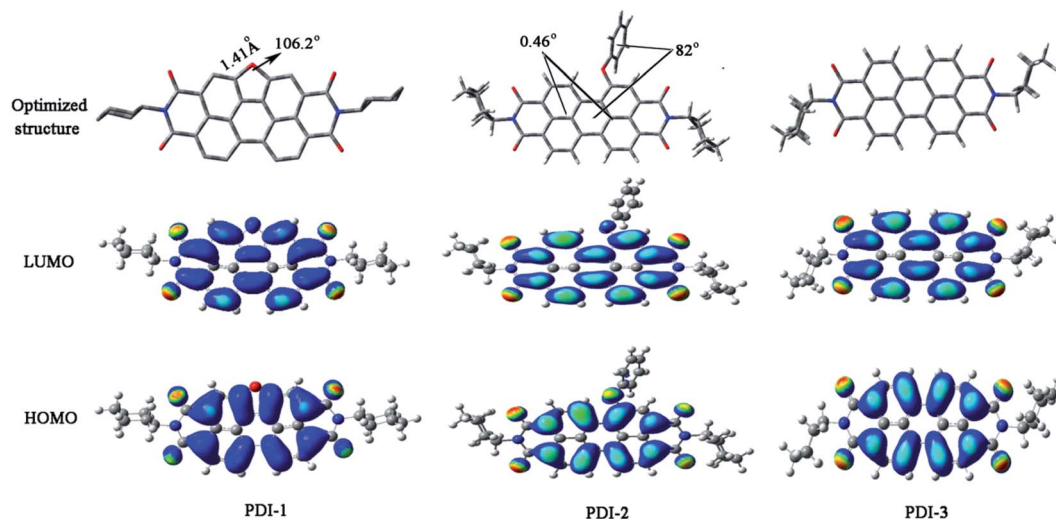
Fig. 4 Optimized structures and computed frontier orbitals of **PDI-1**, **PDI-2**, and **PDI-3** obtained by DFT calculations at the B3LYP/6-31G* level.

PDI-1 has planar conformation. The formation of the O-heterocyclic ring induced the two naphthalene moieties to get far away in the site of open ring and induced the two naphthalene moieties to get close to each other in the site of O-heterocyclic ring. Planar conformation is favorable for the π–π stacking of self-assembled **PDI-1** and covalent interactions between **PDI-1** and TiO_2. **PDI-3** also had a planar conformation. But in **PDI-2**, the introduction of phenol substituent broke the original conformation. The approximate dihedral angle between phenol and perylene core was 82°, and the approximate dihedral angle between the two naphthalene subunits connected to the central benzene ring is 0.46°. The steric hindrance of the phenoxy substituent at bay position prevented the perylene nucleus from contacting TiO_2 and so the interaction between **PDI-2** and TiO_2 was weak. HOMO and LUMO orbital of **PDI-2** and **PDI-3** are mainly distributed on the perylene ring. The phenol group contributes little to the molecular orbital of **PDI-2**. It is worth noting that the HOMO orbital of **PDI-1** is centered at the perylene ring system, while the LUMO orbital is delocalized at the perylene nucleus and oxygen atom site. This is conductive to the electron delocalization from oxygen atom to TiO_2. Moreover, due to the existence of electron-rich O-heterocyclic, **PDI-1** is richer in electron in comparison with **PDI-3**. Thus, **PDI-1** can act as a good hole-transporting layer.[39] The cyclic voltammograms of **PDI-1**, **PDI-2**, and **PDI-3** are illustrated in Fig. S12.† **PDI-1** has two reduction peaks, indicating that it can accept at least two electrons.[40] The HOMO/LUMO energy levels of **PDI-1**, **PDI-2**, and **PDI-3** were estimated to be −6.26/−3.62, −6.52/−4.10, and −6.43/−3.89 eV, respectively. The increased HOMO and LUMO energy level of **PDI-1** would improve its hole-transfer ability.[41] The strong visible absorption, unique planar structure, good solubility, and higher HOMO/LUMO energy level of **PDI-1** indicated that it has good application value in the field of photocatalysis.

The color of pure TiO_2, **PDI-1**, **PDI-2**, **PDI-3**, **PDI-1**/TiO_2, **PDI-2**/TiO_2, and **PDI-3**/TiO_2 are shown in Fig. 5. The pure TiO_2, **PDI-1**, **PDI-2**, and **PDI-3** is white, yellow, dark red, and bright red,

respectively (Fig. 5a, b, c and d), whereas **PDI-1**/TiO_2, **PDI-2**/TiO_2, and **PDI-3**/TiO_2 is butter yellow, pink, and brownish red, respectively (Fig. 5e, f and g).

Fig. 6 shows SEM images of TiO_2, **PDI-1**, **PDI-2**, **PDI-3**, **PDI-1**/TiO_2, **PDI-2**/TiO_2, and **PDI-3**/TiO_2. Fig. 6a and b shows that TiO_2 form uniform spherical particles with diameter of about 500 nm. As can be seen from Fig. 6c, e and g, pure **PDI-1**, **PDI-2**, and **PDI-3** in mixture solution (DCM : MeOH = 1 : 3) formed nanorods (the average width was 200 nm, and the length was in the range of a few tens of micrometers), nanobelts (the average width was 3 μm, and the length was in the range of 300 μm to 500 μm), and amorphous stack structure, respectively. The aggregation of the molecules seemed to be dominated by the PDI rings with substituent at bay position. Despite the different morphologies, both **PDI-1** and **PDI-2** nanostructures formed extended 1D charge carrier pathways (enabled by the π–π stacking) and had large surface areas, making them suitable for the study of comparative photocatalytic. 1D self-assembly of **PDI-1** and **PDI-2** occurred because of their decreased solubilities when a large amount of CH_3OH was injected into their CH_2Cl_2 solutions. The insolubility could drive a strong intrinsic co-facial π–π stacking of the aromatic core (stacking along the long axis) in conjunction with the association between the side chains (aggregating along the short axis). Fig. 6d, f and h could illustrate many features. The sponge-like **PDI-1**, **PDI-2**, or **PDI-3** clusters was uniformly embedded on TiO_2 surface. Fig. 6h clearly shows that particles of **PDI-3**/TiO_2 solid exhibited an uneven spherical structure. Fig. 6d and f demonstrates that **PDI-1**/TiO_2 and **PDI-2**/TiO_2 formed stacking spherical structures

Fig. 5 Photo images of TiO_2 (a), **PDI-1** (b), **PDI-2** (c), **PDI-3** (d), **PDI-1**/TiO_2 (e), **PDI-2**/TiO_2 (f) and **PDI-3**/TiO_2 (g).
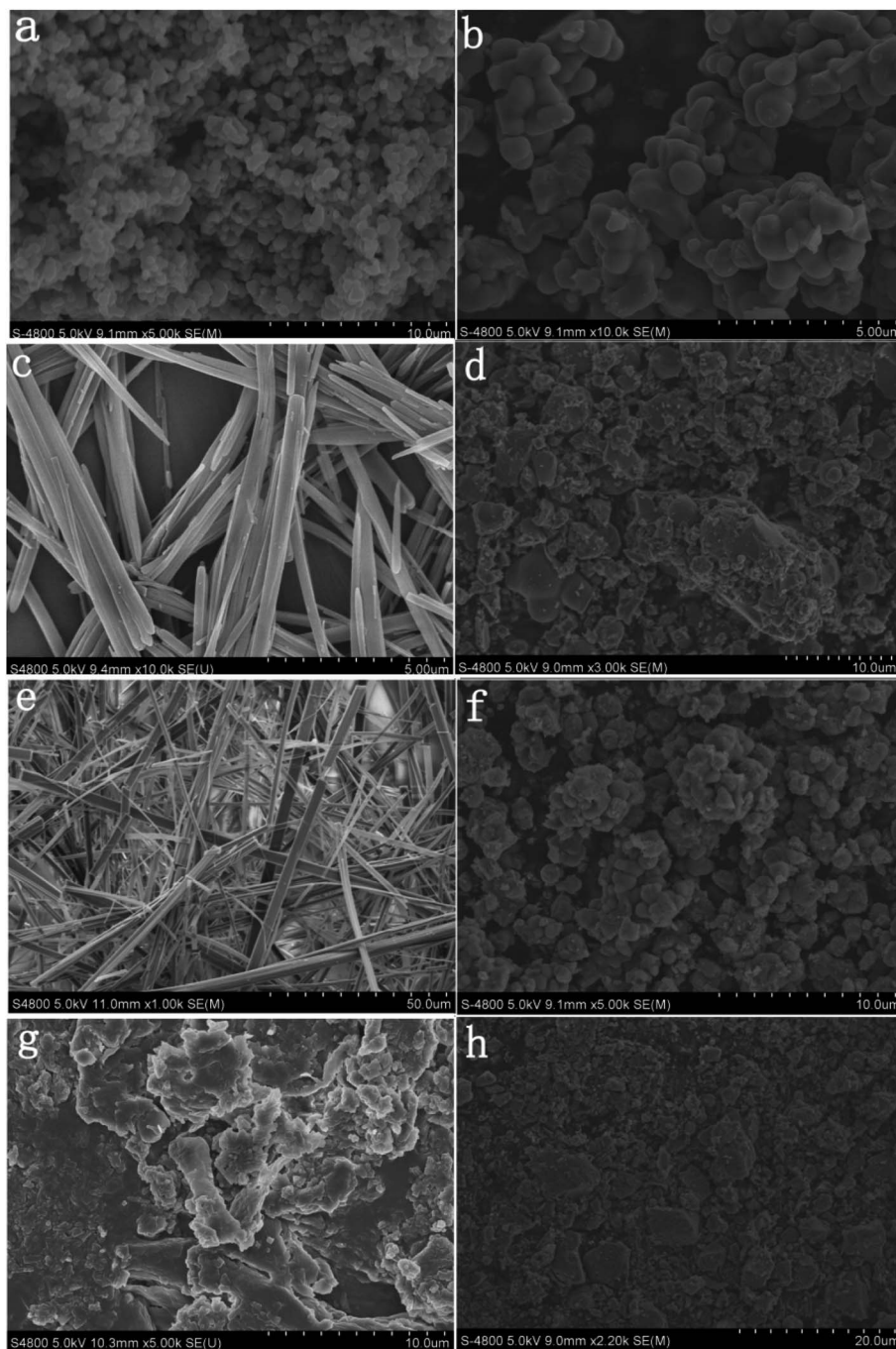
Fig. 6 SEM images of particles of the TiO_2 (a and b), PDI-1/TiO_2 (d), PDI-2/TiO_2 (f), and PDI-3/TiO_2 (h) solid. SEM images of the PDI-1 (c), PDI-2 (e), and PDI-3 (g) in mixture solution (DCM : MeOH = 1 : 3).

with a size of micrometers. Compared with PDI-2/TiO_2 (1 μm), the spherical structure of PDI-1/TiO_2 (2 μm) was thicker. It so happened that the more porous structure can provide more surface active sites.[42] The surface areas of the composites were determined using the nitrogen gas adsorption method. The BET surface area of PDI-1/TiO_2 (92.5 $m^2\,g^{-1}$) was higher than that of PDI-2/TiO_2 (87.4 $m^2\,g^{-1}$) and PDI-3/TiO_2 (82.3 $m^2\,g^{-1}$). Increase of surface area could facilitate dye adsorption and increase photocatalytic activity to some extent.

XRD measurements were performed to determine the crystalline structure of pure TiO_2, PDI-1, PDI-2, PDI-3, PDI-1/TiO_2, PDI-2/TiO_2, and PDI-3/TiO_2 composites (Fig. 7). The crystal phase of TiO_2 in the figure was consistent with the standard card (JCPDF no. 65-5714) (Fig. 7a). This phase could be characterized by the appearance of Bragg diffraction peaks at $2\theta = 25.3°, 37.7°, 48.0°, 53.8°, 55.0°$, and $62.6°$, which were indexed to (101), (004), (200), (105), (211), and (204) planes for TiO_2, respectively.[43] Obviously, the PDI-1/TiO_2 formed an ordered
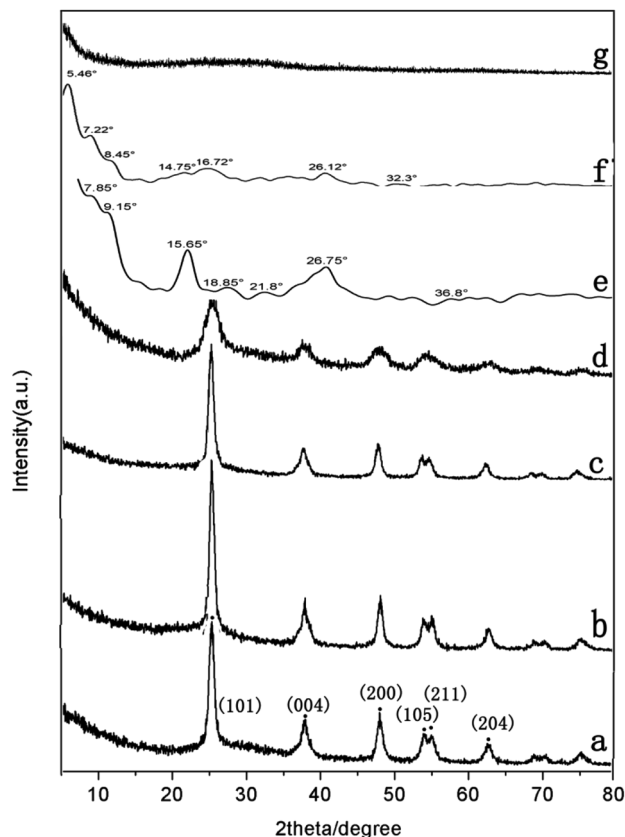
Fig. 7 XRD patterns of (a) pure TiO_2, (b) PDI-1/TiO_2, (c) PDI-2/TiO_2, (d) PDI-3/TiO_2, (e) PDI-1, (f) PDI-2, and (g) PDI-3 composites.
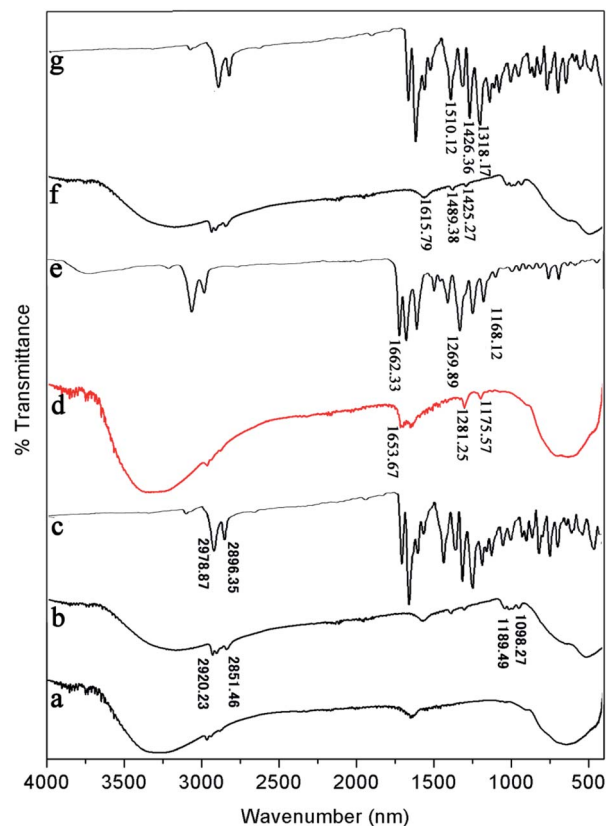

Fig. 8 FT-IR spectra of (a) pure TiO_2, (b) PDI-1/TiO_2, (c) PDI-1, (d) PDI-2/TiO_2, (e) PDI-2, (f) PDI-3/TiO_2, and (g) PDI-3 composites.

structure. Its crystallization property was enhanced in comparison with pure TiO_2, which should be beneficial for its photocatalytic activity.[44] PDI-1/TiO_2, PDI-2/TiO_2, and PDI-3/TiO_2 composites were doped with very little PDI-1, PDI-2, or PDI-3, and so there was no characteristic peak in the XRD of PDI-1/TiO_2 (Fig. 7b), PDI-2/TiO_2 (Fig. 7c), and PDI-3/TiO_2 (Fig. 8d). In the X-ray diffraction pattern of PDI-1, the peak at $2\theta = 26.75°$ (d spacing 3.3 Å) can be attributed to the π–π stacking of the adjacent perylene because the distances of π–π stacking between the perylene cores were approximately 3.5 Å.[45] The intensity of this diffraction peak increased obviously for PDI-1. This result suggests that the π–π stacking interaction of PDI-1 units was powerful, and it was probably because of the unique planar structure of PDI-1 extended the π–π interactions. However, the intensity of this diffraction peak decreased obviously for PDI-2, suggesting that the π–π stacking interaction of PDI-2 units was weak. This is because the phenol substituent weakened the face-to-face arrangement of PDI units. In addition, XRD of PDI-1 showed that the first diffraction peak was 9.15°, the second diffraction peak was 18.85°, and the fourth diffraction peak was 36.8° (Fig. 7e). The multi-order reflections indicate that the self-assembled PDI-1 had well-ordered layered microstructures.[46]

FT-IR was also used to study the surface chemical properties of the composites (Fig. 8). The Ti–O–Ti characteristic absorption peak of TiO_2 was located below 1000 cm^{-1}, and the peak at 3200–3400 cm^{-1} was O–H peak, which was due to a small amount of water on the catalyst surface. The peaks in the range of 1000–1650 cm^{-1} corresponded to the skeleton vibration of PDI-1 benzene ring. The bending vibration peaks of C–H were at 2851 and 2920 cm^{-1}.[47] Compared with the spectrum of pure TiO_2, three new peaks appeared at 1653.67, 1281.25, and 1175.57 cm^{-1} for PDI-2/TiO_2 (and 1615.79, 1489.38, and 1425.27 cm^{-1} for PDI-3/TiO_2). These peaks are characteristic peaks of PDI-2 (PDI-3). Compared with pure PDI-1, PDI-2, or PDI-3, the peaks of PDI-1/TiO_2, PDI-2/TiO_2, or PDI-3/TiO_2 showed apparent shift, which were caused by the force between TiO_2 and self-assembled PDI-1, PDI-2, or PDI-3. These peaks indicated the presence of PDI-1, PDI-2, or PDI-3 in the catalyst composites.

The absorptions of the catalysts were characterized by UV-Vis diffuse reflectance spectra (DRS) (Fig. 9a). UV/vis spectroscopy of the PDI-1/TiO_2 revealed monomeric-dye absorption characteristics of PDI-1. It has absorption peaks identical to a progression of π–π transitions of perylene ring, designated as 0–0 and 0–1. For free monomers, the normal progression of Franck–Condon factor was $A^{0-0} > A^{0-1}$. However, as monomers began to aggregate, the 0–1 transition increased.[48] The 0–1 transition absorption of each of the three composites increased compared to its corresponding PDI monomer. These results suggest that aggregation occurred for PDI-1, PDI-2, or PDI-3 in corresponding catalysts. The band gaps (E_g, eV) of the
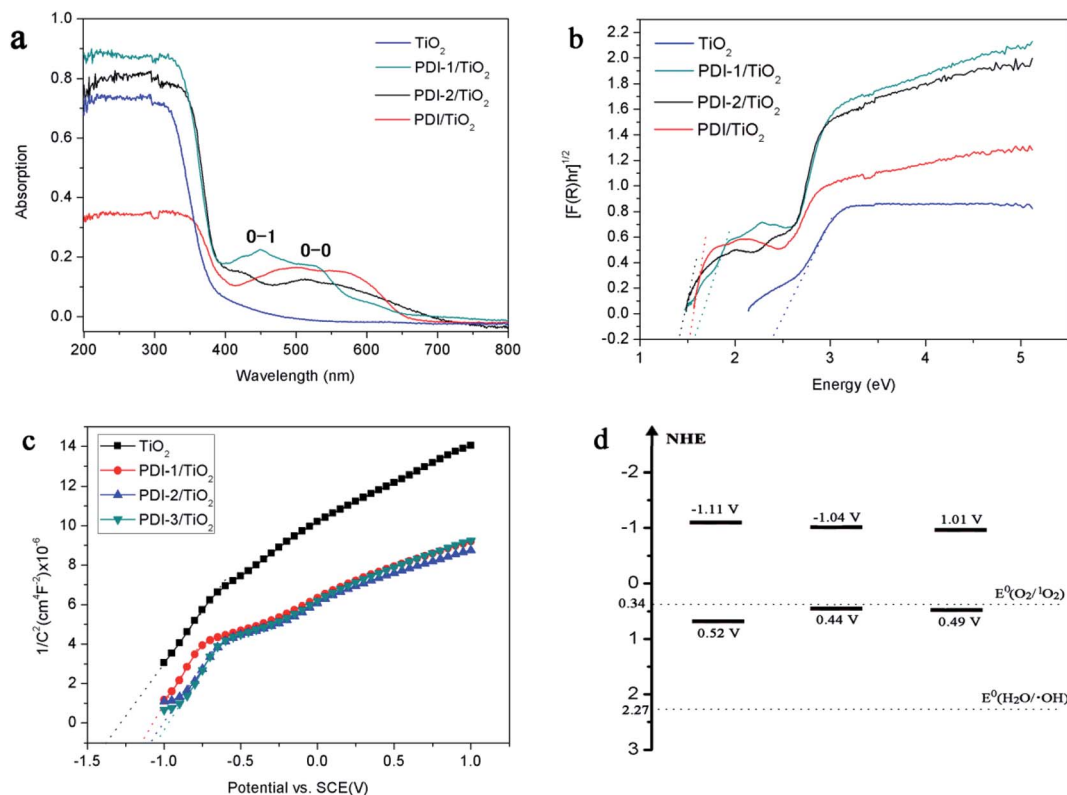
Paper   **RSC Advances**

Fig. 9 (a) DRS spectra, (b) $(F(R)h\nu)^{1/2}$ versus $h\nu$, (c) Mott–Schottky plots, and (d) diagram representing experimentally evaluated VB and CB levels of samples.

composites, by assuming an indirect transition between valence and conduction bands, were calculated using a Tauc equation and Kubelka–Munk function:[49]

$$[F(R)h\nu]^{0.5} = A(h\nu - E_g) \qquad (1)$$

$$F(R) = (1 - R)^2/2R \qquad (2)$$

where $F(R)$ is proportional to the absorption constant, R is the calibrated reflection of samples with $BaSO_4$ reflection, h is the Planck constant, ν is the frequency, A is constant, and E_g is the band gap energy.

The $[F(R)h\nu]^{0.5}$ versus the $h\nu$ is shown in Fig. 9b. E_g value of the samples was obtained by extrapolating the linear part of the plot relating $[F(R)h\nu]^{0.5}$ and $h\nu$ to $[F(R)h\nu]^{0.5} = 0$. The band gaps are found to be 2.39, 1.59, 1.48, and 1.52 eV for TiO_2, **PDI-1**/TiO_2, **PDI-2**/TiO_2, and **PDI-3**/TiO_2, respectively. The increase in UV-visible light absorptions and decrease in band gap energies enhanced the photodegradation efficiency of the catalysts towards MB.

The bottom of conduction band (CB) of TiO_2, **PDI-1**/TiO_2, **PDI-2**/TiO_2, and **PDI-3**/TiO_2 can be estimated by the Mott–Schottky plots. As shown in Fig. 9c, the flat band potential (E_{fb}) of TiO_2, **PDI-1**/TiO_2, **PDI-2**/TiO_2, and **PDI-3**/TiO_2 were −1.37 V, −1.11 V, −1.08 V, and −1.07 V vs. SCE (pH = 7), respectively. For n-type semiconductors, the CB was 0.2 V higher than that of Fermi level. Therefore, the CB of TiO_2, **PDI-1**/TiO_2, **PDI-2**/TiO_2,

and **PDI-3**/TiO_2 under normal hydrogen electrode (NHE, pH = 7) can be calculated using the following equation:

$$E_{CB} \text{ (NHE, pH = 7)} = E_{fb} \text{ (SCE, pH = 7)} + 0.24 - 0.2$$

The results showed that the CB position of TiO_2, **PDI-1**/TiO_2, **PDI-2**/TiO_2, and **PDI-3**/TiO_2 were about −1.33 V, −1.07 V, −1.04 V, and −1.03 V vs. NHE, respectively. According to the band gap (2.39, 1.59, 1.48 and 1.52 eV), the valence band (VB) positions of TiO_2, **PDI-1**/TiO_2, **PDI-2**/TiO_2, and **PDI-3**/TiO_2 were 1.06 V, 0.52 V, 0.44 V, and 0.49 V vs. NHE, respectively. The CB/VB of TiO_2, **PDI-1**/TiO_2, **PDI-2**/TiO_2, and **PDI-3**/TiO_2 were evaluated to be −1.33/1.06 V, −1.11/0.49 V, −1.04/0.32 V, and −1.01/0.44 V. The VB position of **PDI-1**/TiO_2 was deeper than that of **PDI-2**/TiO_2 or **PDI-3**/TiO_2, which means that the oxidation ability of holes of **PDI-1**/TiO_2 is stronger. It was noted that the VB positions of **PDI-1**/TiO_2, **PDI-2**/TiO_2, or **PDI-3**/TiO_2 was shallower than that of hydroxyl radical (2.27 eV),[29] and so it is possible that the hydroxyl radical cannot be generated by **PDI-1**/TiO_2, **PDI-2**/TiO_2, or **PDI-3**/TiO_2. The CB position of singlet oxygen (0.34 eV) was shallower than that of **PDI-1**/TiO_2, **PDI-2**/TiO_2, or **PDI-3**/TiO_2. This result revealed that singlet oxygen may be the main active substance in **PDI-1**/TiO_2 **PDI-2**/TiO_2, or **PDI-3**/TiO_2 composite for photocatalytic degradation of MB.

To further illustrate the chemical state of these composites, X-ray photoelectron spectroscopy (XPS) analysis was carried out
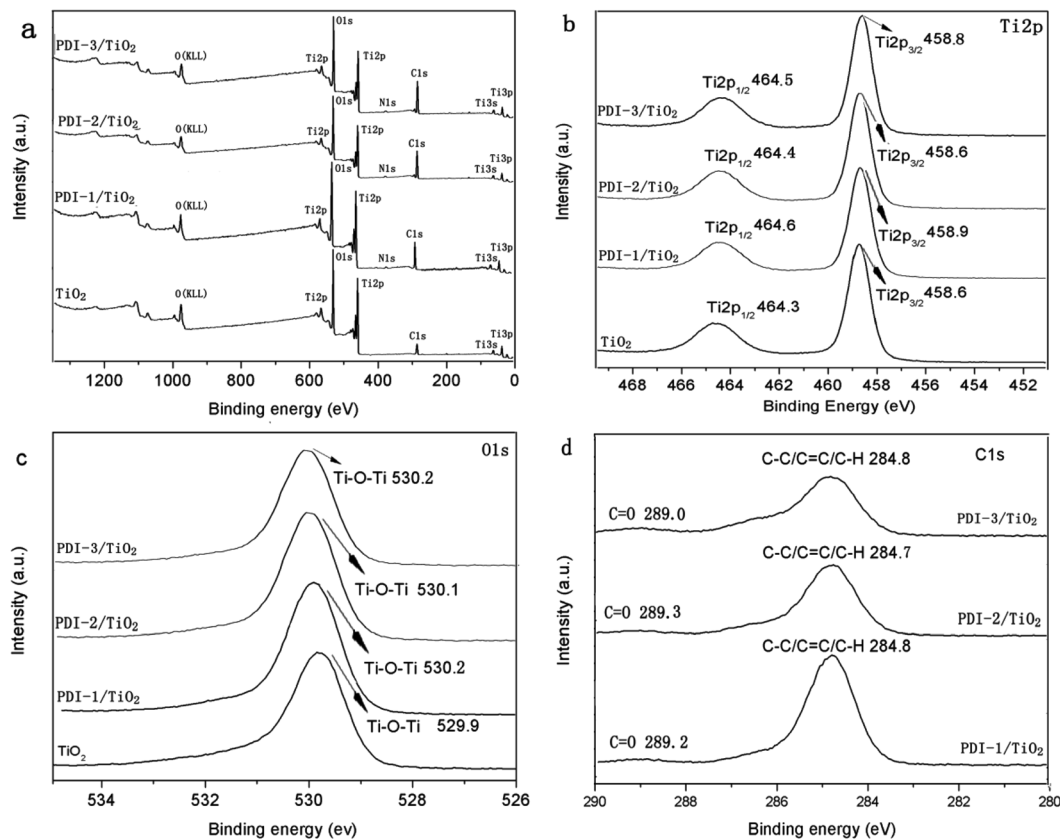
Fig. 10 The XPS spectra of TiO_2, **PDI-1**/TiO_2, **PDI-2**/TiO_2 and **PDI-3**/TiO_2: (a) survey spectra, (b) Ti2p spectra, (c) O1s spectra and (d) C1s spectra.

(Fig. 10). Fig. 10a showed that there were Ti, O, C, and N in these composites. Binding energy peaks of elements Ti, O, and C were shown in Fig. 10b–d, respectively. The Ti2p signal splits into two photoelectron peaks: Ti2p$_{1/2}$ and Ti2p$_{3/2}$, which appeared at the range of 464.3–464.6 eV and 458.6–458.9 eV, respectively.[50] The O1s signal showed contributions at the range of 529.9–530.2 eV, which can be attributed to the O1s binding energy of oxygen in hydroxy group.[51] The C1s spectra (Fig. 10d) showed two peaks with different values: 289.0–289.2 eV and 284.7–284.8 eV, which were identified as C=O and C–C/C=C/C–H functional groups, respectively.[52] Compared with other composites, **PDI-1**/TiO_2 composite had slightly larger binding energy peaks relative to that of pure TiO_2. It indicated that there may be a strong interaction between self-assembled **PDI-1** and TiO_2, which could improve the charge separation efficiency in the system. The weak interaction between **PDI-2** and TiO_2 was due to the steric hindrance of the phenoxy substituent at bay position that prevented the perylene nucleus from contacting TiO_2. Compared with **PDI-1**/TiO_2, **PDI-3**/TiO_2 had a larger Ti2p and O1s binding shift but its degradation efficiency was lower. This is because **PDI-3** was amorphous, whereas **PDI-1** had an ordered nanostructure. Conjugated **PDI-1** can transfer electrons quickly from the semiconductor interior to the surface of TiO_2. This property reduced the recombination of electrons and holes and improved the stability and photocatalytic activity of **PDI-1**/TiO_2.

3.3. Mechanism of enhancement of photocatalytic activity

In order to understand the mechanism of the enhanced photocatalytic activity of **PDI-1**/TiO_2, photoluminescence (PL) spectra of TiO_2, **PDI-1**/TiO_2, **PDI-2**/TiO_2 and **PDI-3**/TiO_2 were investigated. The PL spectra between 350–550 nm of TiO_2, **PDI-1**/TiO_2, **PDI-2**/TiO_2, and **PDI-3**/TiO_2 after excitation at 296 nm are shown in Fig. 11. TiO_2 showed six major emission peaks, which were located at 399, 440, 451, 469, 483, and 492 nm, respectively. The peak at 399 nm was attributed to a direct
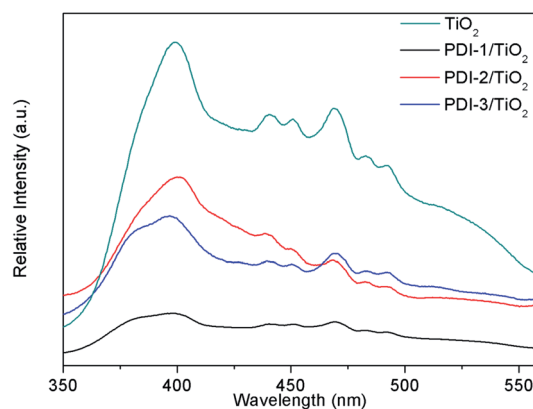

Fig. 11 The photoluminescence spectra of TiO_2, **PDI-1**/TiO_2, **PDI-2**/TiO_2 and **PDI-3**/TiO_2 (λ_{ex} = 296 nm).

transition from the conduction band to the valence band, while the remaining peaks are ascribed to exciton effects resulting from lattice defects and surface states. The PL peaks at 440, 451, and 469 nm were caused by inter-band transitions, and those at 483 and 492 nm were caused by intra-band transitions within the energy level traps or surface states.[53] When **PDI-1** and TiO_2 were hybridized, the fluorescence emission showed a significant reduction. While when **PDI-2** or **PDI-3** was hybridized with TiO_2, the emission intensity only changed slightly. The emission quantum yields (Φ) were 0.092%, 0.017%, 0.063%, 0.051% for TiO_2, **PDI-1**/TiO_2, **PDI-2**/TiO_2, and **PDI-3**/TiO_2, respectively. The results show that coupling of TiO_2 and **PDI-1** benefited electron–hole separation, which weakened the fluorescence intensity and improved the photocatalytic activity of **PDI-1**/TiO_2.

The PL spectra of **PDI-1**/TiO_2, **PDI-2**/TiO_2, and **PDI-3**/TiO_2 after excitation at 493 nm are shown in Fig. 12. The fluorescence intensity of PDIs depended on the density of transition carriers. On the other way, PDIs doping agents and aggregation were the direct factors to increase non-radiative transition, lead to energy loss, and inhibit radiative transition.[26] It was observed that the emission of **PDI-1**/TiO_2 had maximum intensity at 543 nm. The intensity of **PDI-3**/TiO_2 hybrid was relatively lower, while it was higher than that of **PDI-2**/TiO_2. The results indicated that **PDI-1**/TiO_2 had the highest density of transition carriers. To interpret the photophysical properties in a more intuitive manner, the fluorescence lifetimes of **PDI-1**, **PDI-2**, **PDI-3**, **PDI-1**/TiO_2, **PDI-2**/TiO_2, and **PDI-3**/TiO_2 were measured and shown in Fig. S13.† The PDIs and composites had single lifetime and decays were mono-exponential and the average fluorescence lifetimes were 3.41, 3.73, 3.52, 5.51, 5.30, and 5.43 ns, respectively. It was noted that the fluorescence lifetimes of **PDI-1**/TiO_2 was 1.6 times longer than that of **PDI-1**. The addition of TiO_2 would decrease electrons and holes recombination in the interfacial layer of **PDI-1** shell due to ultrafast ET process.

The transient photocurrent responses of TiO_2, **PDI-1**/TiO_2, **PDI-2**/TiO_2, and **PDI-3**/TiO_2 and the corresponding electrochemical impedance (EIS) Nyquist plots are shown in Fig. 13. The photocurrent significantly reduced to 0 as soon as the light
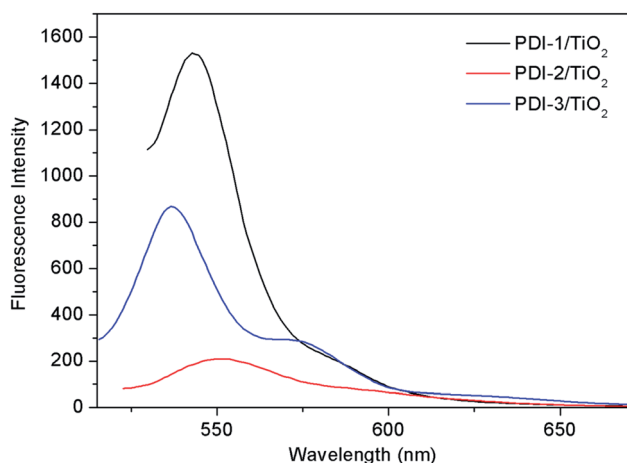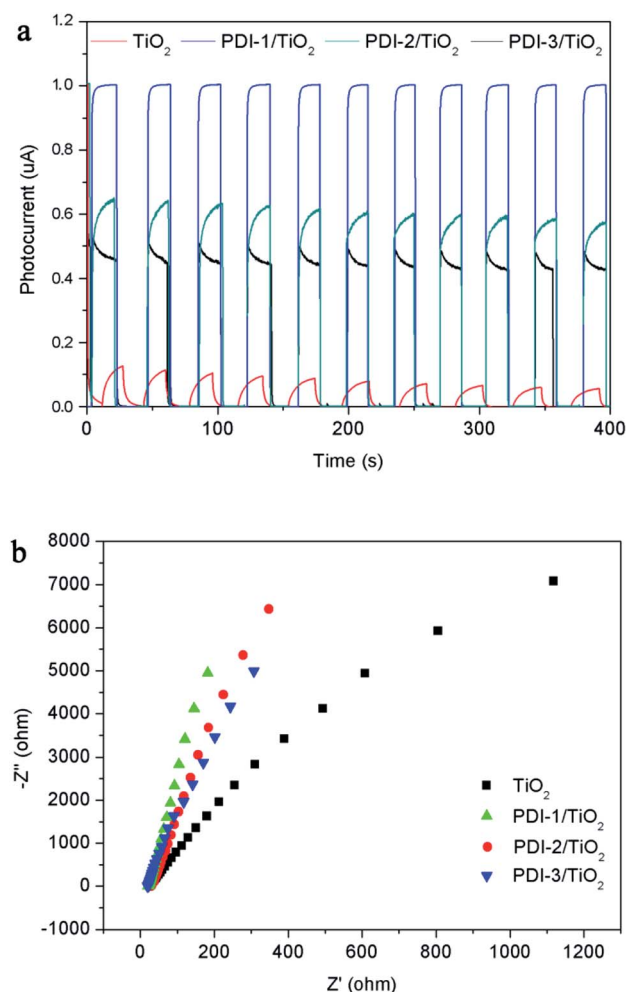

Fig. 13 (a) Photocurrent response and (b) EIS spectra of TiO_2, **PDI-1**/TiO_2, **PDI-2**/TiO_2 and **PDI-3**/TiO_2.

was turned off, and then it increased rapidly when the light was turned on again, which showing excellent stability and repeatability (Fig. 13a). The photocurrent of **PDI-1**/TiO_2 was significantly higher than that of TiO_2, **PDI-2**/TiO_2, and **PDI-3**/TiO_2, indicating that the interfacial electron transfer between photoexcited **PDI-1** and TiO_2 was more effective. Besides, Fig. 13b showed the EIS Nyquist plots of TiO_2, **PDI-1**/TiO_2, **PDI-2**/TiO_2, and **PDI-3**/TiO_2. The larger diameter of the semicircles represented higher impedance and slower interface charge recombination. The **PDI-1**/TiO_2 had a larger diameter of the semicircle than TiO_2, **PDI-2**/TiO_2, or **PDI-3**/TiO_2 in the middle frequency region, indicating that **PDI-1**/TiO_2 had higher impedance and slower interface charge recombination, and thus improving its visible light photocatalytic activity.

The stability of **PDI-1**/TiO_2 in MB degradation process has been tested under visible light through four consecutive cycles (Fig. S14†). After each run, the catalyst was centrifuged, washed with water, and dried in an oven at 100 °C for 1 h for recover. After four runs, 86.4% of the degradation activity still remained. Fig. S15† shows the FT-IR spectra and SEM images of the **PDI-1**/TiO_2 photocatalyst before and after four recycling runs for the

Fig. 12 The photoluminescence spectra of **PDI-1**/TiO_2, **PDI-2**/TiO_2 and **PDI-3**/TiO_2 (λ_{ex} = 493 nm).

photocatalytic degradation of MB under solar irradiation. As can be seen from Fig. S15,† the FT-IR spectra and SEM images of the regenerated photocatalyst are almost the same as that of the fresh photocatalyst. These results indicate that **PDI-1**/TiO$_2$ catalyst has high stability and is reusable.

Hybridization of **PDI-1** with TiO$_2$ improved the absorption and utilization of visible light. The degradation efficiencies of **PDI-1**/TiO$_2$ and **PDI-2**/TiO$_2$ catalysts were better than that of **PDI-3**/TiO$_2$. **PDI-1** nanorods and **PDI-2** nanobelts can extend 1D charge carrier channel by π–π stacking and had large surface area. After hybridization of TiO$_2$, the electron transferred to the TiO$_2$ surface improved the photocatalytic activity of the composites. In this study, **PDI-1** was loaded on the surface of TiO$_2$ by hydrothermal synthesis method to produce an interaction. This made the contact between the two monomers more compacted and reduced the dissolution of **PDI-1** single molecule. The oxygen on the perylene skeleton can also help firming up the stacking of the **PDI-1** with TiO$_2$ through extended π–π interaction and the electrostatic attraction between electron-rich atom O and electron-poor dye MB. Because of the band gap differences between **PDI-1** and TiO$_2$ and the unique structure of **PDI-1**/TiO$_2$, it can absorb MB effectively, transfer charge rapidly, and increase the separation of electrons and holes dramatically. So, the photocatalytic activity of **PDI-1**/TiO$_2$ could be greatly increased. Compared with **PDI-1**/TiO$_2$, **PDI-2**/TiO$_2$ showed high decolorization rate but low degradation efficiency. This is because the steric hindrance of phenoxy substituent at the bay position could prevent the perylene nucleus from contacting TiO$_2$, making the interaction between **PDI-2** and TiO$_2$ weak. So, although the oxygen at the perylene core could absorb MB, **PDI-2**/TiO$_2$ catalyst cannot degrade it effectively.

The **PDI-1** nanostructure had an appropriate thickness so that the electrons excited in the interface layer can be injected into the conduction band of TiO$_2$ to prevent electron–hole recombination. However, if the number of aggregates is excessively large to result in increased thickness and a stack that overlays some of the active sites, the photocatalytic activity will be reduced. Thus, there is a balance between charge separation and light absorption, and 0.01 wt% **PDI-1**/TiO$_2$ might represent the balance point.

The UV-vis spectra of MB (10 mg L^{-1}) solution with **PDI-1**/TiO$_2$ catalyst at different visible irradiation times are shown in Fig. S16.† The spectra shape showed no significant change during irradiation, and the absorption peaks intensity at 291 nm and 664 nm decreased gradually and disappeared eventually. This indicates that the intermediate was not absorbed at the analytical wavelengths and MB was completely degraded.

In order to study the photocatalytic mechanism of **PDI-1**/TiO$_2$ photocatalyst, we used free radical capture experiment to identify active substances in photocatalytic process. Control experiments were carried out using p-benzoquinone (p-BQ) for quenching $\cdot$O$_2^-$, disodium ethylenediamine tetraacetate (EDTA-2Na) for holes, and isopropanol (IPA) for $\cdot$OH, respectively.[54–56] As shown in Fig. 14, when EDTA-2Na was added, the degradation efficiency (16%) of MB with **PDI-1**/TiO$_2$ decreased dramatically, implying that h$^+$ was one of the main active radical in the
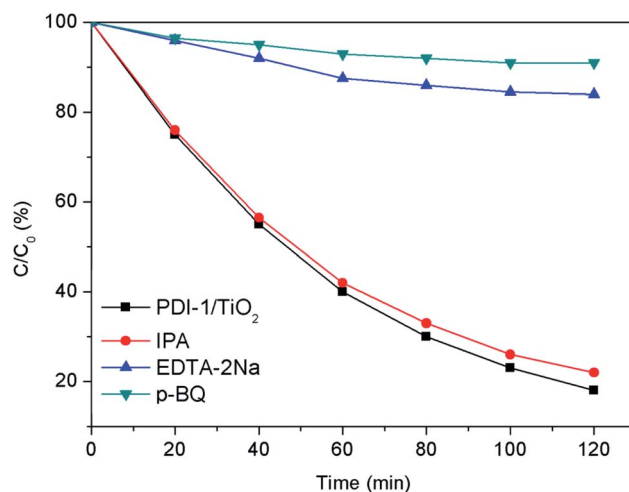

Fig. 14 Plots of photo-generated active species trapped in the system of photodegradation of MB by **PDI-1**/TiO$_2$ under visible light.

photocatalytic degradation process. However, the degradation activity of the catalyst did not decrease after the addition of IPA, indicating that $\cdot$OH was not the main active substances. When p-BQ was added in the reaction system, the degradation rate decreased from 82% to 9%, showing that $\cdot$O$_2^-$ was also one of the main active substances. These data indicated that the main active substances for photocatalytic degradation of MB by **PDI-1**/TiO$_2$ composite were h$^+$ and $\cdot$O$_2^-$.

The HOMO/LUMO energy levels of **PDI-1** obtained by DFT calculations at the B3LYP/6-31G* level are estimated to be −6.26/−3.62. Conduction band of TiO$_2$ (rutile, −4.8 eV; anatase, −5.1 eV (ref. 57)) lies between the HOMO and LUMO levels of **PDI-1**. The HOMO/LUMO energy levels of **PDI-2** and **PDI-3** are estimated to be −6.52/−4.10 and −6.43/−3.89 eV, respectively. **PDI-1** had higher HOMO and LUMO energy levels than **PDI-2** and **PDI-3**, which would improve its hole-transfer ability. Molecular modeling shows that **PDI-1** can reinforce the stacking of the molecules through noncovalent bonding, hydrogen bonding, and extended π–π stacking (Fig. 15). The crystal structure of **PDI-1** exhibited a nearly planar molecular conformation composed of edge-to-face dimers. The dimer was herringbone filled structure with a plane spacing of 3.3 Å. The short planar distance between perylene chromophores facilitate charge carriers hopping from one molecule to the next. Under visible-light illumination, **PDI-1** can be excited to generate electrons and holes. Since the LUMO potential of **PDI-1** is more negative than the CB of TiO$_2$, the photo-generated electrons of **PDI-1** can be injected directly into the CB of TiO$_2$ through the π–π conjugate structure. Some electrons transferred to TiO$_2$ reacted with the pollutants, and some others reacted with O$_2$ adsorbed on the catalyst surface to produce $\cdot$O$_2^-$, which participated in photocatalytic reactions to oxidize pollutants into CO$_2$ and H$_2$O. At the same time, the holes could be easily moved to the surface and oxidize the adsorbed contaminants directly. This significantly increased the activity of the **PDI-1**/TiO$_2$ photocatalyst for MB degradation under visible light.
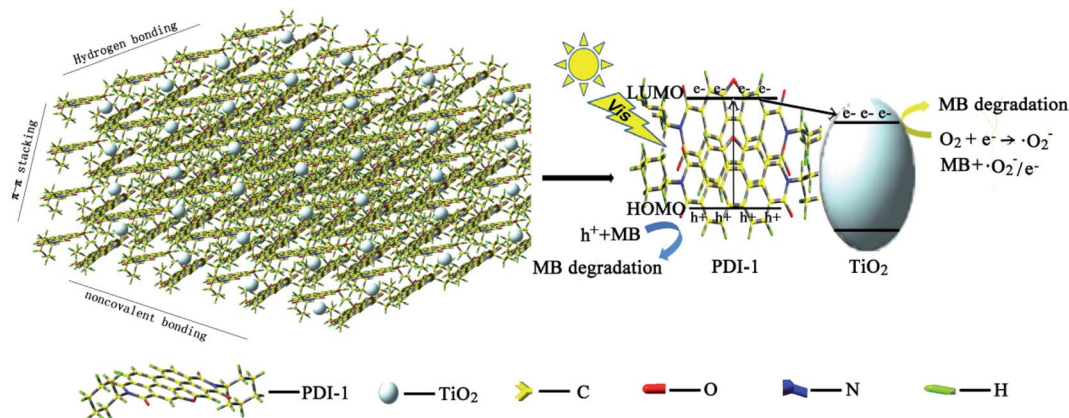
Fig. 15 Photocatalytic degradation mechanism of **PDI-1**/TiO$_2$ composite.

In general, most of the photoelectrons and holes recombined quickly but only some were involved in photocatalytic degradation process. This led to a low quantum efficiency. When **PDI-1** was combined with TiO$_2$, **PDI-1** aggregates acted as light-sensitizers and electrons would be transferred to the surface of TiO$_2$ rapidly through the extended π–π structure in **PDI-1**. The extended π–π structure of **PDI-1** facilitated it to gain good transmission holes performance and to transfer the photo-generated hole to the surface of the composite photocatalyst quickly. This reduced the photo-induced recombination rate of electrons and holes and further improved the photocatalytic activity of the catalyst.

4. Conclusions

Three novel visible-light-driven composite photocatalysts were reported. They were prepared by hydrothermal synthesis method, which made the contact between two monomers more compacted and reduced the dissolution of PDIs single molecule. A series of chemical characterizations and MB degradation experiments showed that **PDI-1**/TiO$_2$ had excellent photocatalytic activity and stability. The extended π–π stacking of self-assembled **PDI-1** and strong interactions between self-assembled **PDI-1** and TiO$_2$ play significant roles in accelerating charge transfer and decreasing the recombination of photogenerated electron–hole pairs. The tests of radical scavengers confirmed that h$^+$ and ·O$_2^-$ were the main active substances for the degradation of MB. The characterization of the doped pigments was achieved using X-ray powder diffraction, DRS spectroscopy, FT-IR spectrum, XRD spectra, and photoluminescence measurements. Valence state and size of the binding energy were analyzed using XPS spectra. This work provides a practical way to improve the performance of traditional organic and inorganic composite photocatalysts by designing nano-structured heterocyclic annulated PDIs doped TiO$_2$ photocatalysts. Also, it provides an efficient way to obtain stable PDIs doped TiO$_2$ photocatalyst by hydrothermal synthesis.

Conflicts of interest

There are no conflicts to declare.

Acknowledgements

References

1 R. K. Gupta and A. A. Sudhakar, Perylene based liquid crystals as materials for organic electronics applications, *Langmuir*, 2019, **35**, 2455–2479.

2 J. D. Schultz, A. F. Coleman, A. Mandal, J. Y. Shin, M. A. Ratner, R. M. Young and M. R. Wasielewski, Steric interactions impact vibronic and vibrational coherences in perylene diimide cyclophanes, *J. Phys. Chem. Lett.*, 2019, **10**, 7498–7504.

3 C. Huang, S. Barlow and S. R. Marder, Perylene-3,4,9,10-tetracarboxylic acid diimides: synthesis, physical properties, and use in organic electronics, *J. Org. Chem.*, 2011, **76**, 2386–2407.

4 R. T. Weitz, K. Amsharov, U. Zschieschang, E. B. Villas, D. K. Goswami, M. Burghard, H. Dosch, M. Jansen, K. Kern and H. Klauk, Organic n-channel transistors based on core-cyanated perylene carboxylic diimide derivatives, *J. Am. Chem. Soc.*, 2008, **130**, 4637–4645.

5 C. Chang, H. Tsai and K. Chen, Green perylene bisimide dyes: synthesis, photophysical and electrochemical properties, *Materials*, 2014, **7**, 5488–5506.

6 F. Würthner, C. R. Saha-Möller, B. Fimmel, S. Ogi, P. Leowanawat and D. Schmidt, Perylene bisimide dye

assemblies as archetype functional supramolecular materials, *Chem. Rev.*, 2016, **116**, 962–1052.

7 C. Li and H. Wonneberger, Perylene imides for organic photovoltaics: yesterday, today, and tomorrow, *Adv. Mater.*, 2012, **24**, 613–636.

8 L. Zang, Y. K. Che and J. S. Moore, One-dimensional self-assembly of planar pi-conjugated molecules: adaptable building blocks for organic nanodevices, *Acc. Chem. Res.*, 2009, **40**, 1596–1608.

9 H. Y. Tsai and K. Y. Chen, 1,7-Diaminoperylene bisimides: synthesis, optical and electrochemical properties, *Dyes Pigm.*, 2013, **96**, 319–327.

10 H. Zhao, Y. Zhang, H. Xu, Z. He, Z. Zhang and H. Zhang, Synthesis and properties of perylene diimide dyes bearing unsymmetrical and symmetrical phenoxy substituents at bay positions, *Tetrahedron*, 2015, **71**, 7752–7757.

11 G. J. Zhao and K. L. Han, Excited state electronic structures and photochemistry of heterocyclic annulated perylene (HAP) materials tuned by heteroatoms: S, Se, N, O, C, Si, and B, *J. Phys. Chem. A*, 2009, **113**, 4788–4794.

12 K. G. Ravindra, D. Anamika, S. Ashish, K. I. Parameswar and A. S. Achalkumar, Heteroatom bay-annulated perylene bisimides: new materials for organic field effect transistors, *ACS Appl. Electron. Mater.*, 2019, **1**, 1378–1386.

13 Y. J. Li, T. F. Liu, H. B. Liu, M. Z. Tian and Y. L. Li, Self-assembly of intramolecular charge-transfer compounds into functional molecular systems, *Acc. Chem. Res.*, 2014, **47**, 1186–1198.

14 X. V. Doorslaer, P. M. Heynderickx, K. Demeestere, K. V. Debevere, H. Langenhove and J. Dewulf, TiO$_2$ mediated heterogeneous photocatalytic degradation of moxifloxacin: operational variables and scavenger study, *Appl. Catal., B*, 2012, **111**, 150–156.

15 P. Raizada, P. Singh, A. Kumar, G. Sharma, B. Pare, S. B. Jonnalagadda and P. Thakur, Solar photocatalytic activity of nano-ZnO supported on activated carbon or brick grain particles: role of adsorption in dye degradation, *Appl. Catal., A*, 2014, **486**, 159–169.

16 W. Lu, T. Xu, Y. Wang, H. Hu, N. Li, X. Jiang and W. Chen, Synergistic photocatalytic properties and mechanism of g-C$_3$N$_4$ coupled with zinc phthalocyanine catalyst under visible light irradiation, *Appl. Catal., B*, 2016, **180**, 20–28.

17 A. Varotto, C. Y. Nam, I. Radivojevic, J. P. C. Tomé, J. A. Cavaleiro, C. T. Black and C. M. Drain, Phthalocyanine blends improve bulk heterojunction solar cells, *J. Am. Chem. Soc.*, 2010, **132**, 2552–2554.

18 H. Wang, L. Zhao, X. Liu, J. Xu, W. Hou, J. Wang, E. He, R. Zhang and H. Zhang, Novel hydrogen bonding composite based on copper phthalocyanine/perylene diimide derivatives p–n heterojunction with improved photocatalytic activity, *Dyes Pigm.*, 2017, **137**, 322–328.

19 S. Chen, C. Wang, B. R. Bunes, Y. Li, C. Wang and L. Zang, Enhancement of visible-light-driven photocatalytic H$_2$ evolution from water over g-C$_3$N$_4$, through combination with perylene diimide aggregates, *Appl. Catal., A*, 2015, **498**, 63–68.

20 A. Ebrahimian, M. A. Zanjanchi, H. Noei, M. Arvand and Y. Wang, TiO$_2$ nanoparticles containing sulphonated cobalt phthalocyanine: preparation, characterization and photocatalytic performance, *J. Environ. Chem. Eng.*, 2014, **2**, 484–494.

21 W. Jiang, Z. Qiu, W. Yao, Y. Zhu and W. Cui, TiO$_2$/Al(H$_2$PO$_4$)$_3$ composite film as separation-free and washing-resistance photocatalyst, *Appl. Catal., B*, 2017, **204**, 43–48.

22 P. Wang, J. Wang, T. Ming, X. Wang, H. Yu, Y. Wang and M. Lei, Dye-sensitization induced visible-light reduction of graphene oxide for the enhanced TiO$_2$ photocatalytic performance, *ACS Appl. Mater. Interfaces*, 2013, **5**, 2924–2929.

23 J. W. Kim, H. S. Kim, K. H. Yu, A. Fujishima and Y. S. Kim, Enhanced photocatalytic activity of 3,4,9,10-perylenetetracarboxylic diimide modified titanium dioxide under visible light irradiation, *Bull. Korean Chem. Soc.*, 2010, **31**, 2849–2853.

24 S. Chen, D. L. Jacobs, J. Xu, Y. Li, C. Wang and L. Zang, 1D nanofiber composites of perylene diimides for visible-light-driven hydrogen evolution from water, *RSC Adv.*, 2014, **4**, 48486–48491.

25 A. Senthilraja, B. Krishnakumar, M. Swaminathan and S. Nagarajan, Self-assembly, photophysical and electrochemical properties and activation of the TiO$_2$ photocatalyst by perylene bisimide, *New J. Chem.*, 2014, **38**, 1573–1580.

26 W. Q. Wei, D. Liu, Z. Wei and Y. F. Zhu, Short-range π–π stacking assembly on P25 TiO$_2$ nanoparticles for enhanced visible-light photocatalysis, *ACS Catal.*, 2017, **7**, 652–663.

27 L. Liu, M. Yue, J. Lu, J. Hu, Y. Liang and W. Cui, The enrichment of photo-catalysis via self-assembly perylenetetracarboxylic acid diimide polymer nanostructures incorporating TiO$_2$ nano-particles, *Appl. Surf. Sci.*, 2018, **456**, 645–656.

28 S. Chen, P. Slattum, C. Wang and L. Zang, Self-assembly of perylene imide molecules into 1D nanostructures: methods, morphologies, and applications, *Chem. Rev.*, 2015, **115**, 11967–11998.

29 J. Wang, D. Liu, Y. Zhu, S. Zhou and S. Guan, Supramolecular packing dominant photocatalytic oxidation and anticancer performance of PDI, *Appl. Catal., B*, 2018, **231**, 251–261.

30 G. Boobalan, P. Imran, C. Manoharan and S. Nagarajan, Fabrication of highly fluorescent perylene bisimide nanofibers through interfacial self-assembly, *J. Colloid Interface Sci.*, 2013, **393**, 377–383.

31 Y. Ma, Z. Shi, A. Zhang, J. Li, X. Wei, T. Jiang, Y. Li and X. Wang, Self-assembly, optical and electrical properties of five membered O- or S-heterocyclic annulated perylene diimides, *Dyes Pigm.*, 2016, **135**, 41–48.

32 F. Zhang, Y. Ma, Y. Chi, H. Yu, Y. Li, T. Jiang, X. Wei and J. Shi, Properties of perylene diimide dyes bearing unsymmetrical substituents at bay position, *Sci. Rep.*, 2018, **8**, 8208–8219.

33 A. D. Becke, Density-functional thermochemistry. III. The role of exact exchange, *J. Phys. Chem.*, 1993, **98**, 5648–5652.

34 K. K. Ong, J. O. Jensen and H. F. Hameka, Theoretical studies of the infrared and Raman spectra of perylene, *J. Mol. Struct.: THEOCHEM*, 1999, **459**, 131–144.

35 A. D. Becke, Density-functional exchange-energy approximation with correct asymptotic behavior, *Phys. Rev. B: Condens. Matter Mater. Phys.*, 1998, **38**, 3098–3100.

36 Y. Ma, F. Zhang, J. Zhang, T. Jiang, X. Li, J. Wu and H. Ren, A water-soluble fluorescent pH probe based on perylene dyes and its application to cell imaging, *Luminescence*, 2016, **31**, 102–107.

37 H. L. Qian, C. M. Liu, Z. H. Wang and D. B. Zhu, S-heterocyclic annelated perylene bisimide: synthesis and co-crystal with pyrene, *Chem. Commun.*, 2006, 4587–4589.

38 Y. Ma, F. Zhang, T. Jiang, H. Ren, X. Wei, Y. Zhu and X. Huang, Photophysical, electrochemical, self-assembly, and molecular packing properties of a sulfur-decorated perylene derivative, *Can. J. Chem.*, 2019, **97**, 780–787.

39 T. Hassheider, S. A. Benning, H. S. Kitzerow, M. F. Achard and H. Bock, Color tuned electroluminescence from columnar liquid crystalline alkyl arenecarboxylates, *Angew. Chem., Int. Ed.*, 2001, **40**, 2060–2063.

40 G. Boobalan, P. M. Imran, S. G. Ramkumar and S. Nagarajan, Fabrication of luminescent perylene bisimide nanorods, *J. Lumin.*, 2014, **146**, 387–393.

41 Y. Jiang, L. Lu, M. Yang, C. Zhan, Z. Xie, F. Verpoort and S. Xiao, Taking the place of perylene diimide: perylene tetracarboxylic tetraester as a building block for polymeric acceptors to achieve higher open circuit voltage in all-polymer bulk heterojunction solar cells, *Polym. Chem.*, 2013, **4**, 5612–5620.

42 J. Wei, J. Wang, J. Zhou, R. Zhang and D. Zhang, Synthesis of $Zn_{0.3}Co_{2.7}O_4$ porous willow leaf like structure for enhanced electrocatalytic oxygen evolution reaction, *Mater. Lett.*, 2017, **198**, 196–200.

43 L. H. Tian, X. D. Yan and X. B. Chen, Electrochemical activity of iron phosphide nanoparticles in hydrogen evolution reaction, *ACS Catal.*, 2016, **6**, 5441–5448.

44 Y. Wei, M. Ma, W. Li, J. Yang, H. Miao, Z. Zhang and Y. Zhu, Enhanced photocatalytic activity of PTCDI-C60 via π–π interaction, *Appl. Catal., B*, 2018, **238**, 302–308.

45 T. V. Boom, R. T. Hayes, Y. Y. Zhao, P. J. Bushard, E. A. Weiss and M. R. Wasielewski, Charge transport in photofunctional nanoparticles self-assembled from zinc 5,10,15,20-tetrakis(perylenediimide)porphyrin building blocks, *J. Am. Chem. Soc.*, 2002, **124**, 9582–9590.

46 T. Miyata and T. Masuko, Morphology of poly(L-lactide) solution-grown crystals, *Polymer*, 1997, **38**, 4003–4009.

47 T. E. Kaiser, H. Wang, V. Stepanenko and F. Wurthner, Supramolecular construction of fluorescent J-aggregates based on hydrogen-bonded perylene dyes, *Angew. Chem., Int. Ed.*, 2007, **119**, 5637–5640.

48 Y. S. Ma, C. H. Wang, Y. J. Zhao, Y. Yu, C. X. Han, X. J. Qiu and Z. Q. Shi, Perylene diimide dyes aggregates: optical properties and packing behavior in solution and solid state, *Supramol. Chem.*, 2007, **19**, 141–149.

49 A. Eshaghi and H. Moradi, Optical and photocatalytic properties of the Fe-doped TiO_2 nanoparticles loaded on the activated carbon, *Adv. Powder Technol.*, 2018, **29**, 1879–1885.

50 W. W. Zhang, H. L. Guo, H. Q. Sun and R. C. Zeng, Constructing ternary polyaniline graphene–TiO_2 hybrids with enhanced photoelectrochemical performance in photogenerated cathodic protection, *Appl. Surf. Sci.*, 2017, **410**, 547–556.

51 L. Kai, S. Gao, Q. Y. Wang, X. Hui, Z. Y. Wang, B. B. Huang, Y. Dai and J. Lu, In-situ-reduced synthesis of Ti^{3+} self-doped TiO_2/g-C_3N_4 heterojunctions with high photocatalytic performance under LED light irradiation, *ACS Appl. Mater. Interfaces*, 2015, **7**, 9023–9030.

52 P. Wang, J. Wang, T. Ming, X. Wang, H. Yu, Y. Wang and M. Lei, Dye-sensitization induced visible-light reduction of graphene oxide for the enhanced TiO_2 photocatalytic performance, *ACS Appl. Mater. Interfaces*, 2013, **5**, 2924–2929.

53 J. Zhou, F. Li, C. Du, J. Liu, Y. Wang, W. Li, G. He and Q. He, Photodegradation performance and recyclability of a porous nitrogen and carbon co-doped TiO_2/activated carbon composite prepared by an extremely fast one-step microwave method, *RSC Adv.*, 2016, **6**, 84457–84463.

54 M. C. Yin, Z. S. Li, J. H. Kou and Z. Zou, Mechanism investigation of visible light-induced degradation in a heterogeneous TiO_2/eosin Y/rhodamine B system, *Environ. Sci. Technol.*, 2009, **43**, 8361–8366.

55 H. Wang, Y. H. Liang, L. Liu, J. S. Hu and W. Q. Cui, Highly ordered TiO_2 nanotube arrays wrapped with g-C_3N_4 nanoparticles for efficient charge separation and increased photoelectrocatalytic degradation of phenol, *J. Hazard. Mater.*, 2018, **344**, 369–380.

56 Z. Zou, J. Ye, K. Sayama and H. Arakawa, Direct splitting of water under visible light irradiation with an oxide semiconductor photocatalyst, *Nature*, 2001, **414**, 625–627.

57 D. O. Scanlon, C. W. Dunnill, J. Buckeridge, S. A. Shevlin, A. J. Logsdail, S. M. Woodley, C. R. Catlow, M. J. Powell, R. G. Palgrave, I. P. Parkin, G. W. Watson, T. W. Keal, P. Sherwood, A. Walsh and A. A. Sokol, Band alignment of rutile and anatase TiO_2, *Nat. Mater.*, 2013, **12**, 798–801.